JOURNAL OF SOLID STATE CHEMISTRY **136,** 103–114 (1998)
ARTICLE NO. SC977666

# Commensurate and Incommensurate Phases in the System $A_4A'Ir_2O_9$ ($A$ = Sr, Ba; $A'$ = Cu, Zn)

Peter D. Battle,*,[1] Graeme R. Blake,* Jeremy Sloan,*,† and Jaap F. Vente*

*Inorganic Chemistry Laboratory, University of Oxford, South Parks Road, Oxford OX1 3QR, England; and †Department of Materials, University of Oxford, Parks Road, Oxford OX1 3PH, England

Received July 17, 1997; in revised form October 15, 1997; accepted October 22, 1997

**The crystal structure of $Sr_4CuIr_2O_9$ is very sensitive to the conditions of synthesis. Prolonged heating of a commensurate trigonal sample prepared at 1120°C leads to the adoption of an incommensurate structure which can be regarded as a composite of two substructures having common unit cell parameters $a$ and $b$ but different parameters $c_1$ and $c_2$. No detectable change in chemical composition accompanies the structural transition, nor do the magnetic properties of the sample change significantly. The structure of the commensurate form has been determined from neutron powder diffraction data collected at 4.5 K (space group $P321$, $a = 9.68540(3)$ Å, $c = 8.04726(6)$ Å). $Ir_2O_9$ octahedral dimers and $CuO_6$ trigonal prisms alternate in chains parallel to $z$, with the Sr cations located between the chains; the $Cu^{2+}$ cations are disordered within the prisms. The incommensurate form has been studied by X-ray diffraction and electron microscopy ($a = 9.7020(6)$ Å, $c_1 = 4.0069(5)$ Å, $c_2 = 2.6993(4)$ Å). The relationship between the commensurate and incommensurate unit cells is discussed ($c \sim 2c_1 \sim 3c_2$). No commensurate $Ba_4A'Ir_2O_9$ phases could be prepared, but incommensurate samples having $A' = Cu$, Zn showed behavior similar to that of $Sr_4CuIr_2O_9$.** 

## INTRODUCTION

There has been a recent upsurge of interest in the solid-state chemistry of ternary and quaternary oxides of the platinum metals. This has been driven largely by the observation that many of these compounds adopt crystal structures which apparently contain 1D chains of transition metal coordination polyhedra, thus introducing the possibility of unusual electronic properties (1), but it has also been driven in part by recent progress in structural chemistry, in particular the recognition that these structures are related to that of perovskite (2). The 2H hexagonal perovskite structure (3) is often thought of as a pseudo-hcp stack of $AO_3$ layers ($A$ is usually an alkaline earth element) with transition metal cations, $B$, occupying octahedral holes between the layers to give the stoichiometry $ABO_3$. This is sometimes conveniently referred to in terms of $A_3O_9$ layers, leading to the stoichiometry $A_3B_3O_9$. It has now been recognized that the structures of many oxides, the stoichiometry of which is not obviously related to that of perovskite, can be considered within the same structural framework if we allow for the inclusion of modified layer types within the stacking sequence. For example, an ordered removal of three oxide ions from an $A_3O_9$ layer leads to the formation of an $A_3O_6$ layer, and the stacking sequence $(A_3O_6)_3(A_3O_9)$ leads to the overall stoichiometry $A_4O_9$. It has recently been shown (4) that this stacking sequence occurs in the crystal structure of $Sr_4Ru_2O_9$ (Fig. 1), with the Ru(V) cations occupying the octahedral sites which are formed between the layers. In addition to these octahedral sites, the hexagonal stacking of $A_3O_6$ layers leads to the creation of cation sites ($A'$) with trigonal prismatic coordination by oxygen. The creation of these sites, which lie within the $A_3O_6$ layers, is made possible by the reduced oxide concentration therein (Fig. 2). The trigonal prismatic sites are unoccupied in $Sr_4Ru_2O_9$. In compounds in which they are occupied, the stoichiometry of the modified layers is properly described as $A_3A'O_6$, where $A$ and $A'$ may be the same element. Other overall stoichiometries can be envisaged if the stacking sequence of $(A_3A'O_6)$ and $(A_3O_9)$ layers is allowed to vary, and the general case may be written as $(A_3A'O_6)_n(A_3O_9)$ (that is an $(A_3O_9)$ layer is inserted after every $n$ $(A_3A'O_6)$ layers); filling the octahedral and trigonal prismatic holes then leads to the composition $A_{3n+3}A'_nB_{n+3}O_{6n+9}$. A number of $n = 1$ phases have been described previously, for example $Ba_6Ni_5O_{15}$ (5) and $Sr_6Co_5O_{15}$ (6) (these phases have $A' = B$), and the first example of an $n = 2$ phase was reported recently by Campa *et al* (7). Strunk (8) prepared an $n = 3$ phase, $Sr_{12}Ni_{7.5}O_{27}$, in which half of the trigonal prismatic sites are occupied by $Ni^{4+}$, and Abraham (9) has succeeded in making the vacancy-free phase $Sr_4Ni_3O_9$. However, examples of this stacking sequence remain relatively few in

[1] To whom correspondence should be addressed.



0022-4596/98 $25.00

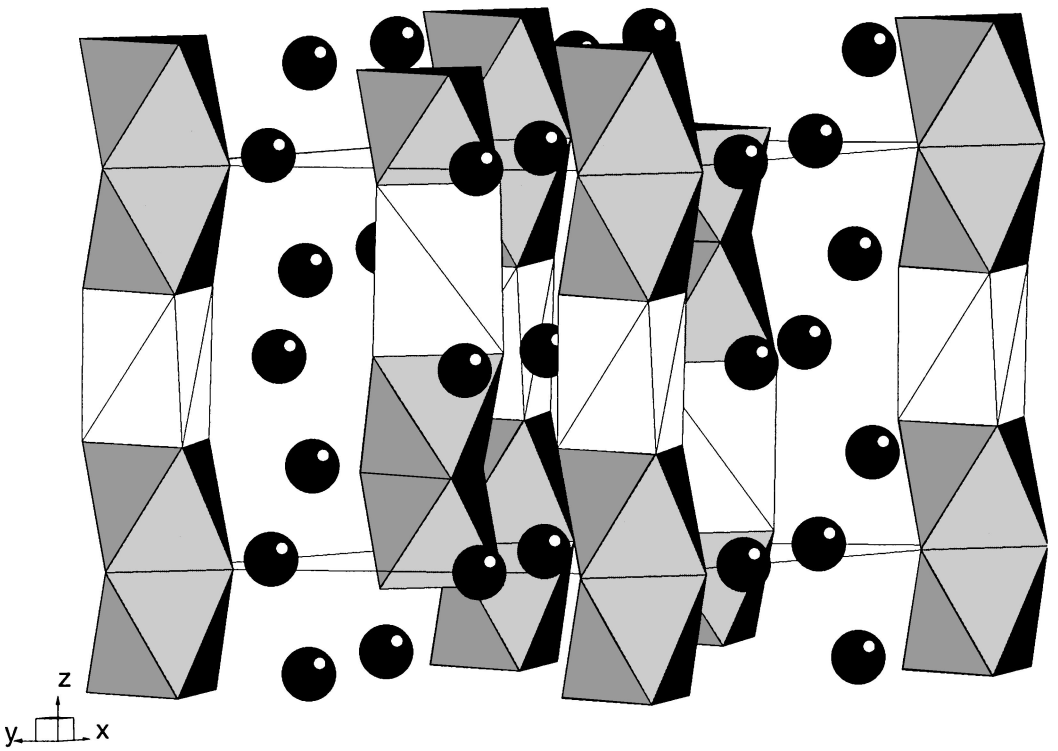


**FIG. 1.** Crystal structure of $Sr_4Ru_2O_9$. $RuO_6$ octahedra are shaded, and empty trigonal prismatic sites are unshaded. Shaded circles represent Sr.

number. We describe below the results of our attempts to extend the range of platinum metals found in this structure to include Ir, and we shall show that, for certain compositions and preparation conditions, the structure must be regarded as an incommensurate composite of two substructures.

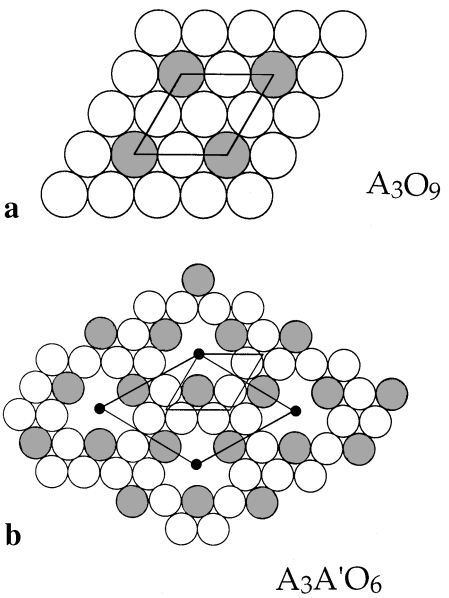


**FIG. 2.** Layers of different stoichiometry in $A_{3n+3}A'_nB_{n+3}O_{6n+9}$: (a) an $A_3O_9$ layer; (b) an $A_3O_6$ layer with trigonal prismatic sites ($A'$) marked by solid circles. The two-dimensional unit cells of both layer types are shown, with $a' = \sqrt{3}a$.

## EXPERIMENTAL

Polycrystalline samples ($\sim$1 g) of nominal composition $A_4A'Ir_2O_9$ ($A$ = Ba, Sr; $A'$ = Cu, Zn) were prepared by firing the appropriate stochiometric quantities of $SrCO_3$, $BaCO_3$, CuO, and ZnO (Johnson Matthey products) in alumina crucibles. Each reaction mixture was initially heated overnight at 800°C and then reground, pelletized, and heated in air at the following temperatures: $Sr_4CuIr_2O_9$ (batch A) 1120°C (5 h); $Sr_4CuIr_2O_9$ (batch B) 1120°C (4 days); $Ba_4CuIr_2O_9$ 1100°C (3 days), 1150°C (5 days), 1200°C (10 days), 1250°C (6 days); $Ba_4ZnIr_2O_9$ 1150°C (2 days), 1200°C (8 days), 1250°C (2 days). The reaction mixtures were reground at frequent intervals. The progress of the reactions was followed by X-ray powder diffraction (XRD) and they were deemed to be complete when the XRD patterns showed the products to be monophasic and to have a high degree of crystallinity. The XRD data were collected using a Siemens D5000 diffractometer, operating over the angular range $5 \leq 2\theta/^\circ \leq 120$ at ambient temperature in Bragg–Brentano geometry with a $2\theta$ step size of 0.02°. The metal content of the products was determined using an Atomscan 25 ICP emission spectrometer, and, where possible, the oxygen content was determined by

thermogravimetric analysis using 10% $H_2/N_2$ as the reducing agent in a Rheometric Scientific STA 1500. The sample was heated from room temperature to 1000°C at a rate of 6°C $min^{-1}$. Further structural characterization of the products was carried out using a 200-kV JEOL 2010 high-resolution transmission electron microscope, equipped with a double-tilt goniometer specimen stage ($\pm 10°$). The microscope has a point resolution of 1.971 Å and the coefficient of spherical aberration ($C_s$) is 0.9. Finely ground specimens were dispersed in chloroform in an ultrasonic bath and then placed, dropwise, onto lacey carbon-coated copper grids (Agar 200 mesh). Lattice images were recorded under optimum Scherzer defocus conditions from crystal fragments aligned with their [010] or [1$\bar{1}$0] zone axes aligned parallel to the electron beam. The rapid onset of beam damage prevented the use of a 400-kV microscope, which would have given enhanced resolution. Image simulations were calculated using the multislice program in the EMS program package (10). A larger sample of $Sr_4CuIr_2O_9$ (A) was prepared for characterization by time-of-flight neutron diffraction. Data were collected in the *d*-spacing range $0.64 \leq d/Å \leq 2.5$ on a sample of mass $\sim 8$ g contained in a cylindrical vanadium can at a temperature of 4.5 K on the instrument HRPD at the ISIS facility, Rutherford Appleton Laboratory. The data were corrected for absorption before analysis by the Rietveld method (11), as implemented in the GSAS program suite (12). A Chebyschev polynomial of the first kind (seven parameters) was used to model the background level, and the peak shape was described by a convolution of back-to-back exponentials and a pseudo-Voigt (five parameters). Magnetic susceptibility measurements were made using a Quantum Design MPMS-5 SQUID magnetometer. Data were collected after cooling the sample, mounted in a gelatin capsule, to 5 K in zero field (ZFC) and also in the measuring field (100 G, FC). Electrical conductivity measurements were attempted using the standard four-probe procedure, a conducting silver paint being used to attach copper wires to a sintered bar of the sample.

**TABLE 1**
**Composition of Compounds $A_4A'Ir_2O_9$ as Determined from ICP Emission Spectroscopy**

| Compound | % *A* (Ba, Sr) obs (calc) | % *A′* (Cu, Zn) obs (calc) | % Ir obs (calc) |
|---|---|---|---|
| $Sr_4CuIr_2O_9$ (A) | 37.06 (37.19) | 6.56 (6.74) | 41.30 (40.79) |
| $Sr_4CuIr_2O_9$ (B) | 39.22 (37.19) | 6.90 (6.74) | 41.50 (40.79) |
| $Ba_4CuIr_2O_9$ | 49.41 (48.13) | 5.43 (5.57) | 34.55 (33.68) |
| $Ba_4ZnIr_2O_9$ | 48.67 (48.05) | 5.78 (5.72) | 35.12 (33.63) |

**TABLE 2**
**Atomic Coordinates of $Sr_4CuIr_2O_9$ (A) at 4.5 K[a]**

| Atom | Site | *x* | *y* | *z* | $U_{iso}$ (Å) |
|---|---|---|---|---|---|
| Sr1 | 6*g* | 0.0226(9) | 0.6890(7) | 0.2539(9) | 0.0106(16) |
| Sr2 | 3*f* | 0.3508(11) | 0 | $\frac{1}{2}$ | 0.0023(19) |
| Sr3 | 3*e* | 0.3256(12) | 0 | 0 | 0.0071(16) |
| Ir1 | 2*d* | 0 | 0 | 0.1614(12) | 0.0054(15) |
| Ir2 | 2*d* | $\frac{1}{3}$ | $\frac{2}{3}$ | 0.0822(11) | 0.0169(19) |
| Ir3 | 2*c* | $\frac{1}{3}$ | $\frac{2}{3}$ | 0.3952(11) | 0.0091(14) |
| Cu1 | 3*f*[b] | 0.9299(15) | 0 | $\frac{1}{2}$ | 0 |
| Cu2 | 6*g*[b] | 0.3771(8) | $\frac{2}{3}$ | 0.7203(12) | 0 |
| O1 | 6*g* | 0.4952(8) | 0.6470(9) | 0.2327(11) | 0.0017(14) |
| O2 | 6*g* | 0.6823(16) | 0.1778(13) | 0.4641(16) | 0.018(2) |
| O3 | 3*e* | 0.8409(14) | 0 | 0 | 0.014(3) |
| O4 | 6*g* | 0.6772(11) | 0.1808(10) | 0.0689(12) | 0.0137(17) |
| O5 | 6*g* | 0.9995(15) | 0.1623(14) | 0.3066(16) | 0.021(2) |

[a]Space group *P*321; $a = 9.68540(3)$ Å, $c = 8.04726(6)$ Å, $V = 653.753(4)$ Å$^3$; $R_{wp} = 3.01\%$, $R_p = 2.35\%$, $\chi^2 = 7.324$.
[b]Occupancy $= \frac{1}{3}$.

## RESULTS

The metal contents of the reaction products, as determined from ICP analysis, are listed in Table 1. The experimental values lead to a stoichiometry close to that expected, that is an $A:A':Ir$ ratio of 4:1:2, and suggest that no significant metal loss has occurred during the synthesis. If this ideal ratio is assumed in calculating the oxygen content from TGA data, then the following compositions result: $Sr_4CuIr_2O_{8.93}$ (A), $Sr_4CuIr_2O_{8.99}$ (B), and $Ba_4CuIr_2O_{9.10}$.

**TABLE 3**
**Selected Bond Distances (Å) and Angles (Deg) for $Sr_4CuIr_2O_9$ (A) at 4.5 K**

| | | | | | |
|---|---|---|---|---|---|
| Ir1–Ir1 | 2.597(19) | Sr1–O1 | 2.777(10) | O3–Ir1–O3 | 82.9(5) × 3 |
| Ir1–Cu1 | 2.808(10) × 3 | | 2.647(10) | O3–Ir1–O5 | 94.3(4) × 3 |
| Ir2–Ir3 | 2.519(13) | Sr1–O2 | 2.521(13) | | 94.5(4) × 3 |
| Ir2–Cu2 | 2.943(12) × 3 | | 2.740(14) | | 176.5(6) × 3 |
| Ir3–Cu2 | 2.650(13) × 3 | Sr1–O3 | 2.590(10) | O5–Ir1–O5 | 88.1(6) × 3 |
| Ir1–O3 | 2.015(12) × 3 | Sr1–O4 | 2.429(12) | O1–Ir2–O1 | 89.1(5) × 3 |
| Ir1–O5 | 1.961(14) × 3 | | 3.046(12) | O1–Ir2–O4 | 91.5(3) × 3 |
| Ir2–O1 | 2.064(10) × 3 | Sr1–O5 | 2.831(15) | | 94.1(3) × 3 |
| Ir2–O4 | 1.955(11) × 3 | | 2.652(15) | | 176.9(5) × 3 |
| Ir3–O1 | 2.122(10) × 3 | Sr2–O1 | 2.612(9) × 2 | O4–Ir2–O4 | 85.4(5) × 3 |
| Ir3–O2 | 1.950(12) × 3 | Sr2–O2 | 2.684(13) × 2 | O1–Ir3–O1 | 86.0(4) × 3 |
| | | | 2.798(16) × 2 | O1–Ir3–O2 | 91.6(4) × 3 |
| Cu1–O5 | 2.071(13) × 2 | Sr2–O5 | 2.397(15) × 2 | | 92.7(4) × 3 |
| | 2.074(11) × 2 | Sr3–O1 | 2.475(10) × 2 | | 177.3(6) × 3 |
| | 2.739(17) × 2 | Sr3–O3 | 2.731(10) × 2 | O2–Ir3–O2 | 89.7(5) × 3 |
| Cu2–O2 | 2.034(13) | Sr3–O4 | 2.768(9) × 2 | | |
| | 2.080(13) | | 3.001(14) × 2 | | |
| | 2.498(13) | Sr3–O5 | 2.929(15) × 2 | | |
| Cu2–O4 | 2.166(12) | | | | |
| | 2.196(12) | | | | |
| | 2.588(12) | | | | |

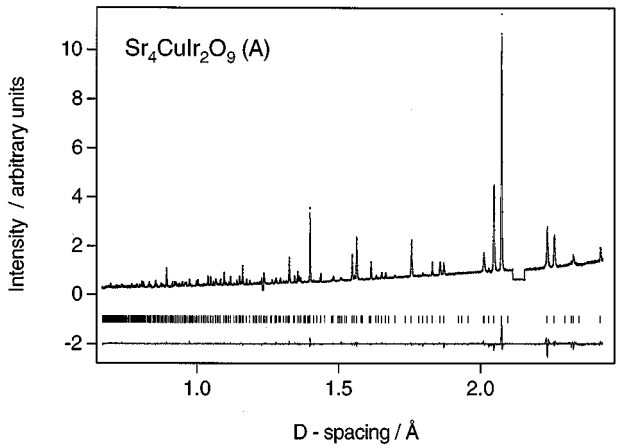


**FIG. 3.** Observed, calculated, and difference neutron diffraction profiles of $Sr_4CuIr_2O_9$ at 4.5 K. Two regions containing cryostat peaks were excluded from the refinements.

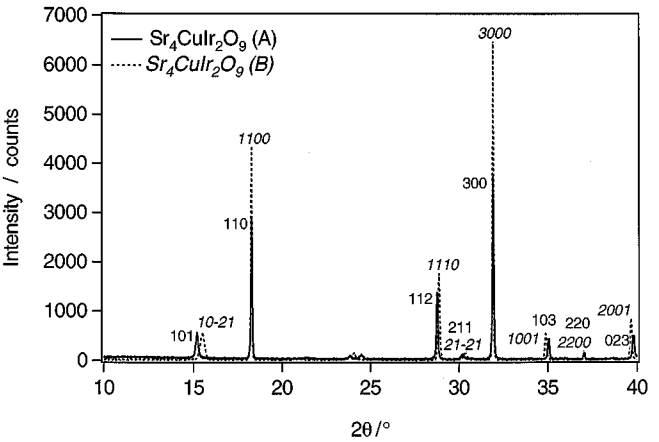


**FIG. 4.** Superposition of the X-ray diffraction patterns of $Sr_4CuIr_2O_9$ (A) and $Sr_4CuIr_2O_9$ (B).

The weight loss in the TGA data collected on $Ba_4ZnIr_2O_9$ had a poorly defined endpoint and an accurate determination of the oxygen content was not possible. The endpoints in the other experiments were better defined, and we estimate that the oxygen contents derived are correct to $\sim 1\%$. The X-ray powder diffraction patterns of $Sr_4CuIr_2O_9$ (A) could be indexed in a trigonal unit cell having $a = 9.7100(2)$ Å and $c = 8.0657(2)$ Å. These values are similar to those found previously for $Sr_4Ru_2O_9$ (4) and are therefore consistent with the formation of an $n = 3$ structure. This compound was selected for detailed study by neutron diffraction. The structure was refined in space group $P321$, using a starting model based on the structure of $Sr_4Ni_{2.5}O_9$ (8). The Ir cations were assigned to the octahedral sites and the Cu cations to the trigonal prismatic sites.

**TABLE 4**
**X-Ray Powder Diffraction Data for $Sr_4CuIr_2O_9$ (B) at Room Temperature ($a = 9.7020(6)$ Å, $c_1 = 4.0069(5)$ Å, $c_2 = 2.6993(4)$ Å)**

| $h$ | $k$ | $l$ | $m$ | $d_{obs}$ | $I_{obs}$ | $d_{calc}$ | $h$ | $k$ | $l$ | $m$ | $d_{obs}$ | $I_{obs}$ | $d_{calc}$ |
|---|---|---|---|---|---|---|---|---|---|---|---|---|---|
| 1 | 0 | −2 | 1 | 5.7109 | 8.88 | 5.7053 | 2 | 4 | −2 | 1 | 1.5558 | 0.94 | 1.5557 |
| 1 | 1 | 0 | 0 | 4.8525 | 66.44 | 4.8510 | 2 | 2 | 2 | 0 | 1.5446 | 2.67 | 1.5447 |
| 1 | 1 | −4 | 3 | 4.2482 | 0.79 | 4.2528 | 5 | 1 | −2 | 1 | 1.4818 | 0.82 | 1.4814 |
| 0 | 2 | −2 | 1 | 3.7005 | 2.17 | 3.6957 | 0 | 5 | 0 | 1 | 1.4265 | 2.20 | 1.4266 |
| 1 | 1 | 1 | 0 | 3.0903 | 27.18 | 3.0893 | 6 | 0 | 0 | 0 | 1.4002 | 6.56 | 1.4004 |
| 2 | 1 | −2 | 1 | 2.9413 | 2.85 | 2.9398 | 2 | 4 | 0 | 1 | 1.3686 | 1.73 | 1.3686 |
| 3 | 0 | 0 | 0 | 2.8007 | 100 | 2.8007 | 4 | 3 | −2 | 1 | 1.3600 | 0.94 | 1.3600 |
| 1 | 0 | 0 | 1 | 2.5691 | 8.32 | 2.5699 | 4 | 1 | 2 | 0 | 1.3525 | 2.59 | 1.3526 |
| 2 | 2 | 0 | 0 | 2.4259 | 3.44 | 2.4255 | 5 | 2 | 0 | 0 | 1.3455 | 2.05 | 1.3454 |
| 0 | 2 | 0 | 1 | 2.2711 | 13.13 | 2.2709 | 0 | 1 | 0 | 2 | 1.3323 | 0.82 | 1.3326 |
| 1 | 3 | −1 | 1 | 2.2425 | 1.91 | 2.2430 | 5 | 1 | 0 | 1 | 1.3171 | 1.74 | 1.3172 |
| 1 | 3 | −2 | 1 | 2.2321 | 3.17 | 2.2322 | 2 | 0 | 0 | 2 | 1.2855 | 0.97 | 1.2850 |
| 2 | 2 | 1 | 0 | 2.0746 | 16.80 | 2.0750 | 5 | 2 | 1 | 0 | 1.2754 | 1.68 | 1.2754 |
| 2 | 1 | 0 | 1 | 2.0571 | 17.00 | 2.0567 | 1 | 2 | 0 | 2 | 1.2419 | 0.91 | 1.2421 |
| 4 | 0 | −2 | 1 | 2.0287 | 2.13 | 2.2078 | 4 | 3 | 0 | 1 | 1.2296 | 1.05 | 1.2297 |
| 0 | 0 | 2 | 0 | 2.0032 | 0.91 | 2.0035 | 5 | 2 | 2 | 0 | 1.1169 | 1.39 | 1.1169 |
| 1 | 1 | 2 | 0 | 1.8515 | 3.73 | 1.8517 | 7 | 1 | 0 | 0 | 1.1128 | 0.85 | 1.1129 |
| 4 | 1 | 0 | 0 | 1.8330 | 5.66 | 1.8335 | 2 | 3 | 0 | 2 | 1.1059 | 0.71 | 1.1056 |
| 1 | 3 | 0 | 1 | 1.7636 | 6.24 | 1.7639 | 3 | 5 | 0 | 1 | 1.0967 | 1.85 | 1.0968 |
| 4 | 1 | 1 | 0 | 1.6673 | 5.32 | 1.6672 | 7 | 0 | 0 | 1 | 1.0967 | 1.85 | 1.0968 |
| 4 | 0 | 0 | 1 | 1.6576 | 2.03 | 1.6577 | 7 | 1 | 1 | 0 | 1.0724 | 0.74 | 1.0723 |
| 3 | 3 | 0 | 0 | 1.6171 | 10.03 | 1.6170 | 6 | 2 | 0 | 1 | 1.0697 | 1.14 | 1.0698 |
| 3 | 2 | 0 | 1 | 1.5686 | 6.67 | 1.5687 | 6 | 3 | 0 | 0 | 1.0585 | 2.17 | 1.0586 |

This approach had only limited success, and a difference Fourier was calculated to identify misplaced atoms. This showed that the model was essentially correct but suggested that the Cu cations are displaced from the 1*b* and 2*d* sites at the centers of the two types of crystallographically distinct trigonal prisms and that they move toward the rectangular faces of these polyhedra. In subsequent analyses these atoms were therefore moved off the 3-fold axes which pass through the prisms, thus introducing disorder into the structure. The temperature factors of the Cu atoms were held fixed at zero, but the variable coordinates of the $3f(x, 0, \frac{1}{2})$ and $6g(x, \frac{2}{3}, z)$ positions were included in the refinement, which involved a total of 24 atomic coordinates and 11 isotropic temperature factors. This strategy produced a significant improvement in the agreement between the observed and calculated diffraction profiles ($R_{wpr} = 3.01\%$, $\chi^2 = 7.32$ (12)); the refined atomic coordinates are presented in Table 2, with the most important bond lengths and bond angles listed in Table 3. The diffraction profiles are plotted in Fig. 3.

Attempts to index the XRD data on $Sr_4CuIr_2O_9$ (B), $Ba_4CuIr_2O_9$, and $Ba_4ZnIr_2O_9$ were initially unsuccessful, even though the data looked very similar to those collected from $Sr_4CuIr_2O_9$ (A). This is illustrated in Fig. 4, which shows the superposition of data from the two samples of $Sr_4CuIr_2O_9$. The $\{hk0\}$ reflections in both patterns show trigonal symmetry and overlie each other, thus allowing the calculation of the unit cell parameter $a$ ($= b$). However, reflections with $l \neq 0$ in pattern B are shifted to both higher and lower $d$-spacings than the corresponding peaks

**TABLE 5**
**X-Ray Powder Diffraction Data for $Ba_4CuIr_2O_9$ at Room Temperature ($a = 10.142(1)$ Å, $c_1 = 4.2411(7)$ Å, $c_2 = 2.7356(4)$ Å)**

| *h* | *k* | *l* | *m* | $d_{obs}$ | $I_{obs}$ | $d_{calc}$ | *h* | *k* | *l* | *m* | $d_{obs}$ | $I_{obs}$ | $d_{calc}$ |
|---|---|---|---|---|---|---|---|---|---|---|---|---|---|
| 1 | 0 | −2 | 1 | 6.4370 | 8.23 | 6.4277 | 4 | 2 | −2 | 2 | 1.5250 | 1.19 | 1.5444 |
| 1 | 1 | 0 | 0 | 5.0789 | 22.21 | 5.0710 | 0 | 5 | 0 | 1 | 1.4784 | 5.62 | 1.4781 |
| 0 | 1 | −4 | 2 | 4.1550 | 2.10 | 4.1549 | 6 | 0 | 0 | 0 | 1.4641 | 16.70 | 1.4639 |
| 1 | 1 | −4 | 3 | 4.0039 | 1.39 | 4.0016 | 3 | 4 | −3 | 2 | 1.4435 | 1.39 | 1.4431 |
| 0 | 1 | −2 | 2 | 3.5318 | 1.68 | 3.5286 | 6 | 0 | −4 | 3 | 1.4281 | 2.92 | 1.4283 |
| 1 | 1 | 1 | 0 | 3.2535 | 69.20 | 3.2533 | 4 | 1 | 2 | 0 | 1.4222 | 10.73 | 1.4219 |
| 2 | 1 | −2 | 1 | 3.1333 | 3.98 | 3.1314 | 5 | 2 | 0 | 0 | 1.4071 | 2.59 | 1.4064 |
| 2 | 1 | −1 | 1 | 3.0540 | 1.17 | 3.0489 | 2 | 0 | −6 | 2 | 1.3881 | 1.39 | 1.3878 |
| 3 | 0 | 0 | 0 | 2.9282 | 100 | 2.9277 | 3 | 4 | −4 | 2 | 1.3811 | 1.59 | 1.3807 |
| 1 | 2 | −4 | 2 | 2.7164 | 1.19 | 2.7146 | 1 | 3 | 1 | 1 | 1.3734 | 1.66 | 1.3734 |
| 1 | 1 | −6 | 3 | 2.6720 | 1.57 | 2.6720 | 5 | 1 | 0 | 1 | 1.3668 | 4.73 | 1.3666 |
| 1 | 0 | 0 | 1 | 2.6121 | 11.31 | 2.6119 | 1 | 1 | 3 | 0 | 1.3618 | 5.11 | 1.3618 |
| 2 | 2 | 0 | 0 | 2.5350 | 1.68 | 2.5355 | 0 | 1 | 0 | 2 | 1.3517 | 2.74 | 1.3515 |
| 3 | 1 | −3 | 2 | 2.4333 | 1.50 | 2.4320 | 5 | 2 | 1 | 0 | 1.3349 | 9.51 | 1.3350 |
| 1 | 3 | −2 | 1 | 2.3598 | 8.23 | 2.3586 | 1 | 6 | −2 | 1 | 1.3261 | 2.52 | 1.3261 |
| 0 | 2 | 0 | 1 | 2.3221 | 21.59 | 2.3220 | 3 | 3 | 2 | 0 | 1.3217 | 2.70 | 1.3218 |
| 2 | 1 | −3 | 1 | 2.1942 | 1.62 | 2.1949 | 2 | 0 | 0 | 2 | 1.3060 | 2.74 | 1.3059 |
| 2 | 2 | 1 | 0 | 2.1767 | 47.54 | 2.1762 | 3 | 2 | 1 | 1 | 1.2827 | 1.44 | 1.2826 |
| 3 | 1 | −4 | 2 | 2.1638 | 1.84 | 2.1643 | 4 | 3 | 0 | 1 | 1.2771 | 2.41 | 1.2770 |
| 4 | 0 | −2 | 1 | 2.1390 | 3.85 | 2.1386 | 1 | 2 | 0 | 2 | 1.2646 | 3.36 | 1.2647 |
| 0 | 0 | 2 | 0 | 2.1221 | 4.8 | 2.1206 | 7 | 0 | −2 | 1 | 1.2437 | 1.97 | 1.2438 |
| 2 | 1 | 0 | 1 | 2.1116 | 30.55 | 2.1112 | 3 | 5 | −2 | 1 | 1.2437 | 1.97 | 1.2438 |
| 3 | 1 | −2 | 2 | 2.0593 | 1.84 | 2.0590 | 2 | 2 | 3 | 0 | 1.2347 | 3.30 | 1.2347 |
| 0 | 4 | −4 | 2 | 1.9912 | 1.24 | 1.9906 | 4 | 4 | 1 | 0 | 1.2148 | 3.67 | 1.2146 |
| 1 | 1 | 2 | 0 | 1.9566 | 13.14 | 1.9564 | 6 | 0 | 2 | 0 | 1.2047 | 2.12 | 1.2047 |
| 4 | 1 | 0 | 0 | 1.9173 | 3.56 | 1.9167 | 3 | 1 | 0 | 2 | 1.1928 | 2.30 | 1.1927 |
| 4 | 1 | −4 | 3 | 1.8389 | 1.35 | 1.8387 | 1 | 0 | 2 | 1 | 1.1837 | 1.50 | 1.1837 |
| 1 | 3 | 0 | 1 | 1.8195 | 13.34 | 1.8193 | 5 | 2 | 2 | 0 | 1.1722 | 6.31 | 1.1721 |
| 4 | 1 | 1 | 0 | 1.7467 | 25.33 | 1.7466 | 7 | 0 | 0 | 1 | 1.1407 | 5.66 | 1.1405 |
| 3 | 0 | 2 | 0 | 1.7171 | 7.70 | 1.7174 | 3 | 5 | 0 | 1 | 1.1407 | 5.66 | 1.1405 |
| 3 | 3 | 0 | 0 | 1.6907 | 20.88 | 1.6903 | 4 | 1 | 3 | 0 | 1.1379 | 4.47 | 1.1377 |
| 2 | 4 | −2 | 1 | 1.6347 | 2.83 | 1.6348 | 2 | 3 | 0 | 2 | 1.1318 | 2.79 | 1.1317 |
| 2 | 2 | 2 | 0 | 1.6272 | 11.17 | 1.6266 | 2 | 1 | 2 | 1 | 1.1243 | 1.53 | 1.1240 |
| 3 | 2 | 0 | 1 | 1.6226 | 18.14 | 1.6224 | 7 | 1 | 1 | 0 | 1.1219 | 3.69 | 1.1219 |
| 4 | 2 | −4 | 2 | 1.5659 | 1.11 | 1.5657 | 6 | 1 | −1 | 2 | 1.1165 | 1.50 | 1.1161 |
| 5 | 1 | −2 | 1 | 1.5562 | 1.75 | 1.5559 | 6 | 2 | 0 | 1 | 1.1128 | 4.31 | 1.1129 |
| 5 | 1 | −1 | 1 | 1.5456 | 1.66 | 1.5455 | 6 | 3 | 0 | 0 | 1.1068 | 8.69 | 1.1066 |

in pattern A, thus preventing the determination of a unique value of $c$. To index these patterns it was necessary to assume that all three samples are incommensurate along [001]. The observed Bragg peaks could then be accounted for using three unit cell parameters ($a$, $c_1$, $c_2$) and four Miller indices ($h$, $k$, $l$, $m$), the $d$-spacing of the $\{hklm\}$ reflection being given by

$$\frac{1}{d^2} = \frac{4}{3a^2}(h^2 + hk + k^2) + \frac{(l + mc_1/c_2)^2}{c_1^2}$$

The success of this indexing strategy suggests that there are two trigonal substructures present in each compound, with unit cell parameters ($a = b, c_1$) and ($a = b, c_2$); the composite structure formed appears incommensurate because $c_1/c_2$ is not a rational fraction. The diffraction data on these phases are listed in Tables 4–6.

The results of our electron microscopy confirm the interpretation of the XRD and give further insight into the nature of these materials, despite the fact that all were beam sensitive and began to deteriorate after only a few minutes in the microscope. As a consequence of this we were not able to record data of equal quality on all specimens, and the results described below are necessarily selective. We were able to obtain diffraction patterns from the [010] and [1$\bar{1}$0] zones of $Sr_4CuIr_2O_9$ (A). The latter is shown in Fig. 5a. Neither of these patterns showed any anomalies and both were consistent with the indexing of the X-ray and neutron diffraction data in space group $P321$. The difference between commensurate and incommensurate $A_4CuIr_2O_9$ can be seen by comparing Fig. 5a with Fig. 5b; the latter shows the [1$\bar{1}$0] zone of $Ba_4CuIr_2O_9$, with a pair of satellite reflections lying close to each principal diffraction spot. All the satellite spots could be accounted for using the four unit cell parameters deduced from the X-ray diffraction data. Figure 6 shows [1$\bar{1}$0] lattice images of $Sr_4CuIr_2O_9$ (A) and $Ba_4CuIr_2O_9$. A simulation of one part of the image of the commensurate, Sr-containing phase is also shown; it was calculated using a defocus of $-500$ Å and a foil thickness of 34 Å. The observed and calculated images are very similar, thus confirming the validity of our structural model. Neither image shows the contrast modulation along [001] that is apparent (arrowed) in the incommensurate Ba compound. Data on a second, somewhat unrepresentative crystal of $Sr_4CuIr_2O_9$ (A) are shown in Fig. 7. The [010] lattice image (Fig. 7a) shows that this particular crystal is twinned; the arrows parallel to [001] indicate the direction of the twin boundaries. The diagonal arrows indicate parallel lines of light and dark contrast caused by the variation in electron density between $Ir_2O_9$ dimers and $CuO_6$ prisms. The corresponding diffraction pattern

**TABLE 6**
**X-Ray Powder Diffraction Data for $Ba_4ZnIr_2O_9$ at Room Temperature ($a = 10.1415(10)$ Å, $c_1 = 4.2429(8)$ Å, $c_2 = 2.7394(5)$ Å)**

| $h$ | $k$ | $l$ | $m$ | $d_{obs}$ | $I_{obs}$ | $d_{calc}$ | $h$ | $k$ | $l$ | $m$ | $d_{obs}$ | $I_{obs}$ | $d_{calc}$ |
|---|---|---|---|---|---|---|---|---|---|---|---|---|---|
| 1 | 0 | −2 | 1 | 6.4254 | 5.49 | 6.4189 | 5 | 2 | 0 | 0 | 1.4064 | 2.07 | 1.4064 |
| 1 | 1 | 0 | 0 | 5.0711 | 24.87 | 5.0708 | 1 | 3 | 1 | 1 | 1.3742 | 0.81 | 1.3744 |
| 0 | 1 | −4 | 2 | 4.1538 | 0.83 | 4.1455 | 5 | 1 | 0 | 1 | 1.3669 | 2.91 | 1.3670 |
| 0 | 2 | −2 | 1 | 3.9881 | 0.86 | 3.9790 | 1 | 1 | 3 | 0 | 1.3624 | 1.70 | 1.3623 |
| 1 | 1 | 1 | 0 | 3.2531 | 49.99 | 3.2540 | 3 | 4 | −2 | 2 | 1.3527 | 1.37 | 1.3521 |
| 2 | 1 | −2 | 1 | 3.1300 | 1.56 | 3.1303 | 5 | 2 | 1 | 0 | 1.3347 | 5.11 | 1.3349 |
| 3 | 0 | 0 | 0 | 2.9269 | 100 | 2.9276 | 3 | 3 | 2 | 0 | 1.3213 | 1.37 | 1.3220 |
| 1 | 0 | 0 | 1 | 2.6153 | 6.51 | 2.6151 | 2 | 0 | 0 | 2 | 1.3067 | 1.80 | 1.3076 |
| 2 | 2 | 0 | 0 | 2.5356 | 1.78 | 2.5354 | 4 | 3 | 0 | 1 | 1.2771 | 1.75 | 1.2773 |
| 1 | 3 | −2 | 1 | 2.3584 | 2.85 | 2.3581 | 1 | 2 | 0 | 2 | 1.2656 | 1.43 | 1.2662 |
| 0 | 2 | 0 | 1 | 2.3233 | 13.97 | 2.3242 | 2 | 2 | 3 | 0 | 1.2352 | 1.43 | 1.2351 |
| 2 | 2 | 1 | 0 | 2.1766 | 27.08 | 2.1764 | 4 | 4 | 1 | 0 | 1.2145 | 2.34 | 1.2146 |
| 4 | 0 | −2 | 1 | 2.1376 | 1.59 | 2.1382 | 6 | 0 | 2 | 0 | 1.2041 | 1.32 | 1.2048 |
| 2 | 1 | 0 | 1 | 2.1129 | 17.39 | 2.1129 | 3 | 1 | 0 | 2 | 1.1937 | 1.21 | 1.1939 |
| 1 | 1 | 2 | 0 | 1.9569 | 6.59 | 1.9571 | 1 | 0 | 2 | 1 | 1.1849 | 0.97 | 1.1846 |
| 4 | 1 | 0 | 0 | 1.9168 | 3.71 | 1.9166 | 5 | 2 | 2 | 0 | 1.1722 | 2.05 | 1.1722 |
| 1 | 3 | 0 | 1 | 1.8201 | 7.89 | 1.8204 | 7 | 1 | 0 | 0 | 1.1630 | 1.32 | 1.1633 |
| 4 | 1 | 1 | 0 | 1.7463 | 14.24 | 1.7466 | 7 | 0 | 0 | 1 | 1.1404 | 3.12 | 1.1407 |
| 3 | 0 | 2 | 0 | 1.7167 | 3.88 | 1.7174 | 3 | 5 | 0 | 1 | 1.1404 | 3.12 | 1.1407 |
| 3 | 3 | 0 | 0 | 1.6901 | 16.37 | 1.6903 | 4 | 1 | 3 | 0 | 1.1376 | 1.67 | 1.1380 |
| 3 | 2 | 0 | 1 | 1.6232 | 10.23 | 1.6231 | 2 | 3 | 0 | 2 | 1.1324 | 1.59 | 1.1328 |
| 0 | 5 | 0 | 1 | 1.4784 | 3.18 | 1.4781 | 7 | 1 | 1 | 0 | 1.1217 | 2.37 | 1.1219 |
| 6 | 0 | 0 | 0 | 1.4637 | 10.52 | 1.4638 | 6 | 2 | 0 | 1 | 1.1128 | 2.64 | 1.1129 |
| 4 | 1 | 2 | 0 | 1.4212 | 4.68 | 1.4221 | 6 | 3 | 0 | 0 | 1.1065 | 5.44 | 1.1065 |

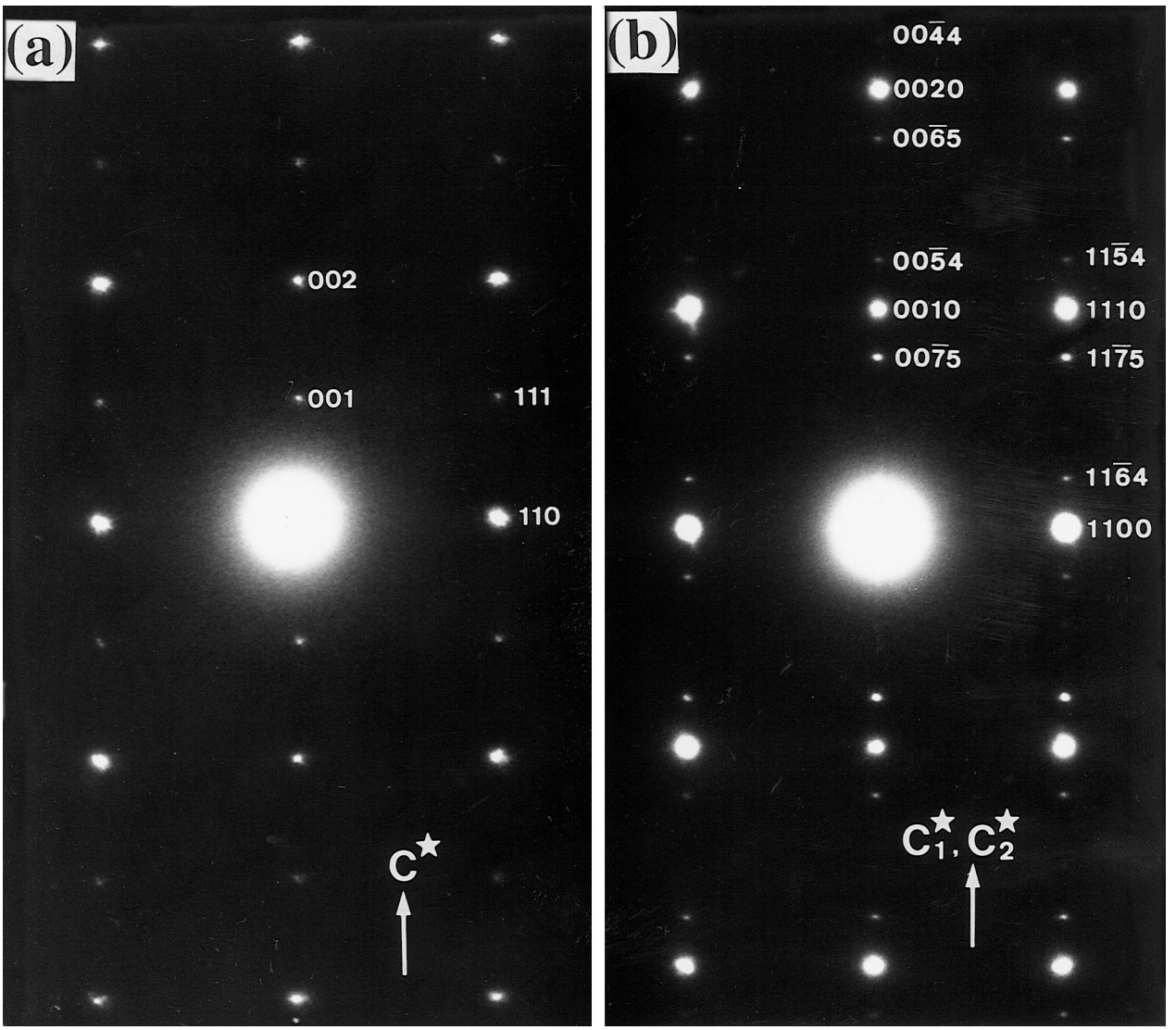


**FIG. 5.** [1$\bar{1}$0] zone electron diffraction patterns of (a) commensurate $Sr_4CuIr_2O_9$ (A) and (b) incommensurate $Ba_4CuIr_2O_9$.

(Fig. 7b) shows diffuse streaking caused by the twinning. The lattice image and the relatively low intensity of the streaking both indicate that the population of twins is quite small, even in this fragment. Fig. 7c shows a magnified view of one of the twin boundaries, and the image either side of the boundary is simulated in Figs. 7d, and 7e, using a defocus of $-380$ Å and a foil thickness of 19 Å. The agreement between observed and calculated images is again good. A schematic representation of the crystal structure at a twin boundary, again viewed along [010], is given in Fig. 8; the arrows in this diagram correspond to those in Fig. 7a.

The structural characterization of our successful preparations is described in detail above, but we did also attempt to prepare several other phases. XRD patterns showed clear evidence for the formation of incommensurate phases having the nominal compositions $Sr_4NiIr_2O_9$, $Sr_4ZnIr_2O_9$, and $Ba_4NiIr_2O_9$, but we were unable to obtain single-phase samples. The X-ray diffraction patterns of our Sr-containing products continued to change with further heating and we were able to deduce that the $n = \infty$ phase $Sr_3A'IrO_6$ is the thermodynamic product in the Sr–$A'$–Ir–O system. This phase forms within 24 h at temperatures of 1300°C or above and over a period of several days at lower temperatures. It coexists with $Sr_2IrO_4$ in the ratio required by the stoichiometry of the initial reaction mixture. We were unable to prepare commensurate samples of the Ba-containing samples described above by varying the synthesis

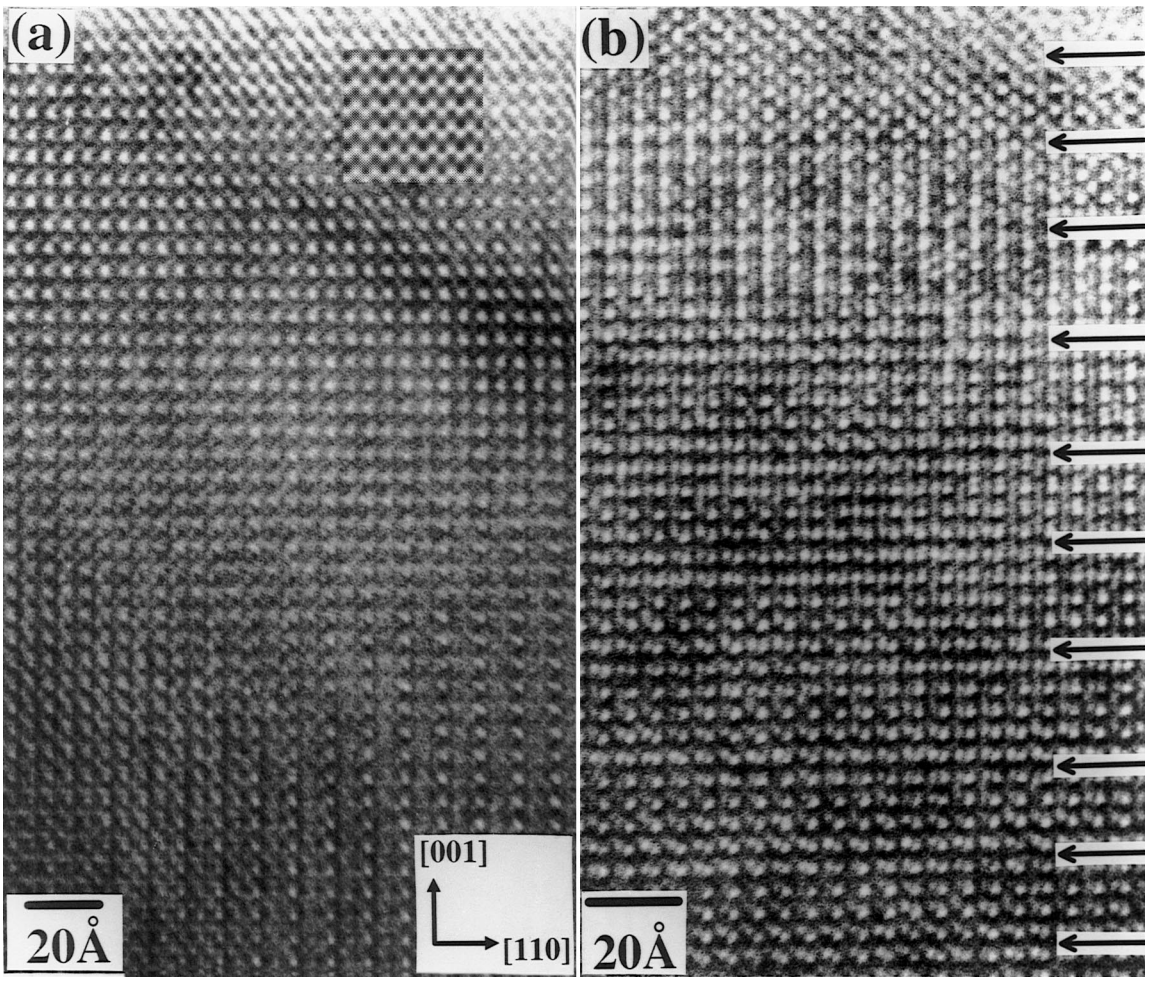


**FIG. 6.** [$1\bar{1}0$] lattice images of (a) $Sr_4CuIr_2O_9$ (A) and (b) $Ba_4CuIr_2O_9$. A simulated image is included with the former, and contrast modulations along [001] are arrowed in the latter. They are best viewed at a glancing angle.

conditions, although we never saw any evidence for the formation of $Ba_3A'IrO_6$.

The inverse molar magnetic susceptibilities of our reaction products are plotted in Fig. 9. No hysteresis is apparent between the ZFC and FC data, which were fitted to a Curie-Weiss law with allowance for an additional temperature-independent (TIP) contribution to the susceptibility;

$$\chi_M = \frac{C}{T-\theta} + \alpha.$$

The fit is good for all four compounds in the temperature range $100 \leq T/K < 300$ and for all but $Ba_4CuIr_2O_9$ throughout the range $5 \leq T/K < 300$. The derived values of $C$, $\theta$, and $\alpha$ are given in Table 7. The values of the Curie constant indicate the presence of one unpaired electron per formula unit in the Cu-containing compounds. The fact that the room temperature susceptibility of $Ba_4ZnIr_2O_9$ is almost completely accounted for by the TIP term suggests that this unpaired electron is associated with the $Cu^{2+}$ cations and that spin-pairing of the $Ir^{4+}$ cations in the $Ir_2O_9$ dimers is essentially complete at 300 K. The magnitude of $\theta$ suggests that antiferromagnetic intercation interactions involving $Cu^{2+}$ are only significant in the case of $Ba_4CuIr_2O_9$. Difficulties in preparing suitable sintered pellets prevented a full study of the electrical conductivity of these compounds, but we were able to measure a value of $3 \times 10^{-5}\,\Omega^{-1}cm^{-1}$ for $Sr_4CuIr_2O_9$ (A) at room temperature; the value became immeasurably small on cooling.

## DISCUSSION

This work is primarily concerned with the structural properties of $A_4A'Ir_2O_9$ phases. However, before discussing

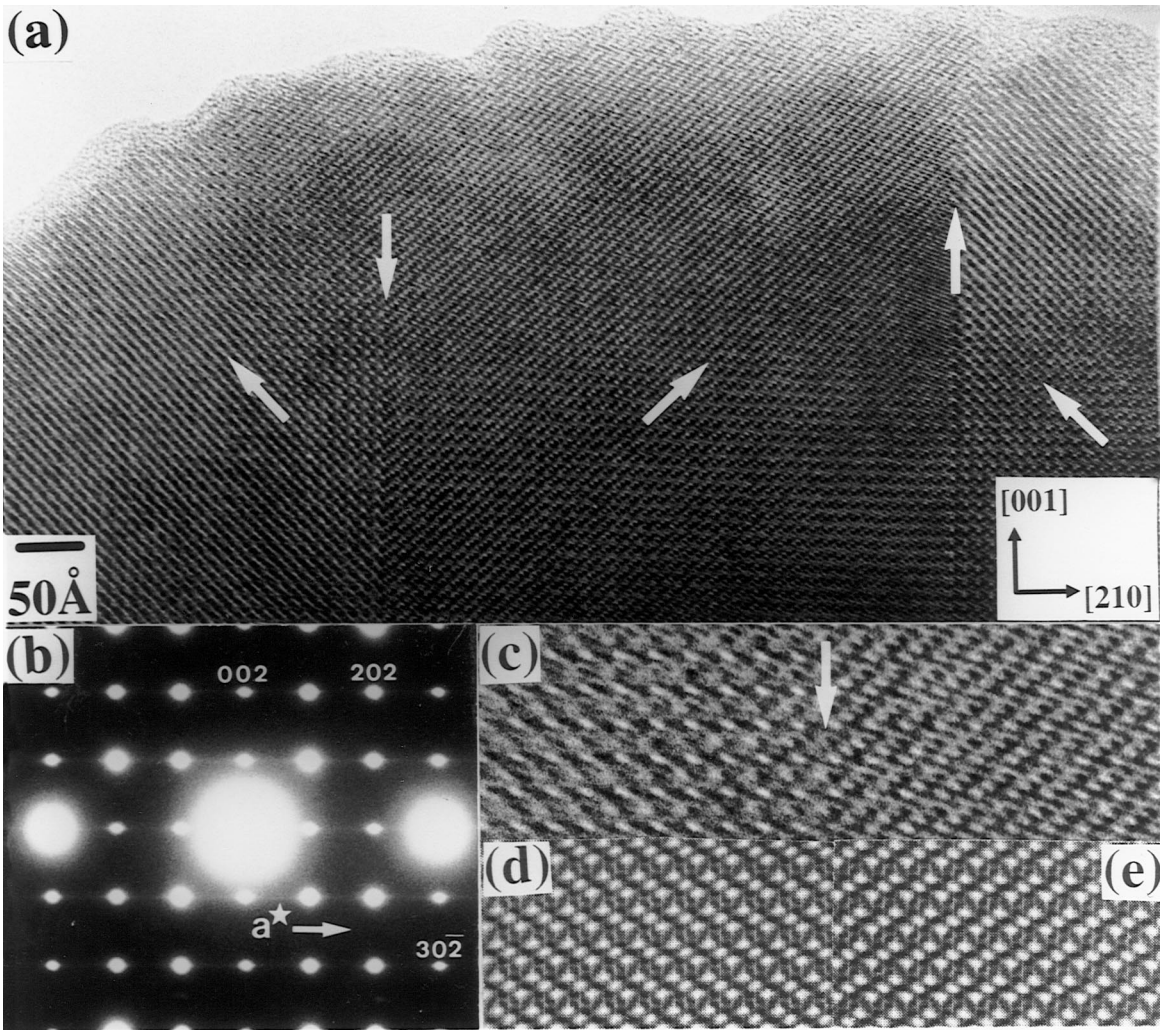


**FIG. 7.** [010] micrographs of twin boundaries in $Sr_4CuIr_2O_9$ (A): (a) lattice image with twin boundaries indicated by arrows parallel to [001]; diagonal arrows indicate parallel lines of light and dark contrast; (b) electron diffraction showing streaking caused by twinning; (c) magnified image of a twin boundary; (d, e) simulated image of the crystal to the (left, right) of the twin boundary.

these in detail, we note that our susceptibility measurements, and the one conductivity measurement that we were able to make, are consistent with these materials having localized electrons in the outer *d* levels. The susceptibility of $Ba_4CuIr_2O_9$ is not as well modeled as those of the other compositions and, in the absence of more complete structural information, we are unable to account for the different behavior of this incommensurate phase.

The crystal structure of $Sr_4CuIr_2O_9$ (A), the only commensurate phase described above, is very similar to that of $Sr_4Ni_3O_9$ (9). It can be described in terms of $Sr_3O_9$ layers and $Sr_3CuO_6$ layers, or it can be considered to consist of alternating $Ir_2O_9$ dimers and $CuO_6$ prisms, sharing faces to form chains parallel to the *z* axis; the space between the chains is occupied by the Sr atoms. There are two crystallographically distinct types of chain (Fig. 10). One involves the cations Ir1 and Cu1 (Table 2) and the anions O3 and O5, whereas the other involves Ir2, Ir3, Cu2, O1, O2, and O4. The unique Ir site in the former leads to a narrower range of bond lengths, but the average distances in the two chains are similar, for example Ir1–Cu1 = 2.808 Å, Ir2–Cu2 = 2.943 Å, and Ir3–Cu2 = 2.650 Å. The mean Ir–O distance within each octahedron is comparable to the distances found in previous neutron diffraction studies of Ir(IV) oxides (13, 14), and the relative elongation of the Ir–O distances involving oxide ions (O1, O3) in the shared faces of the $Ir_2O_9$ dimers is to be expected in view of the mutual repulsion of the highly charged cations through the common face. The short Ir–Ir distances within the $Ir_2O_9$ dimers are consistent with the observation of spin-pairing at

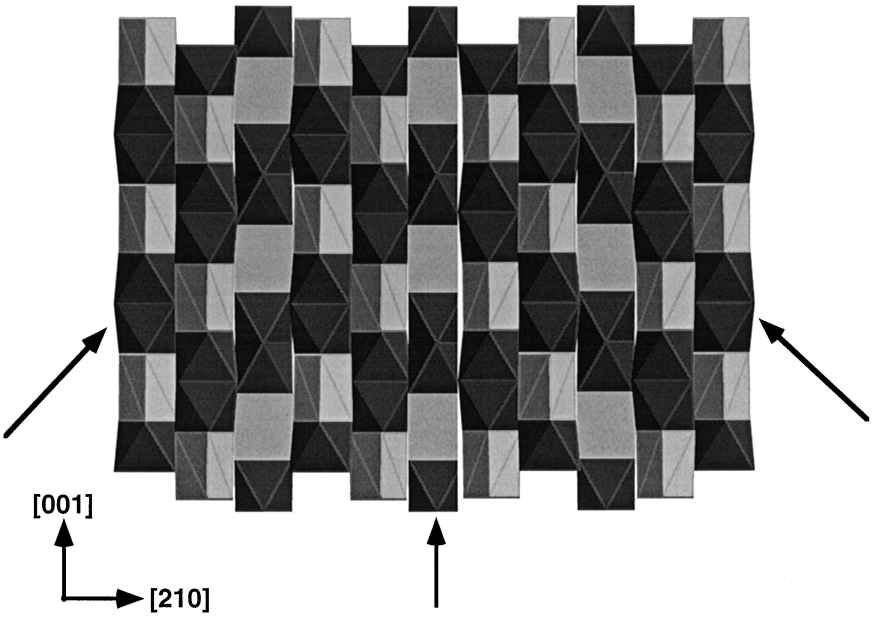


**FIG. 8.** Schematic view, along [010], of the proposed crystal structure of $Sr_4CuIr_2O_9$ (A) at a twin boundary parallel to [001] (arrowed). Diagonal arrows correspond to those in Fig. 7a.

room temperature (15). Our description of the disorder in the trigonal prisms differs slightly from the model used by Abraham, but the general principle is the same. The site is essentially too large for a $Cu^{2+}$ cation to reside at the center of the prism, but it can achieve a satisfactory coordination environment by moving toward the rectangular face of the prism. Figure 10 shows that Cu1 lies almost in the face, whereas Cu2 does not undergo such a large displacement. The environment of Cu1 is more regular than that of Cu2, but both can be considered to be four-coordinate, paramagnetic $Cu^{2+}$ cations. A similar structural feature has been seen previously in the $n = \infty$ compound $Sr_3CuIrO_6$ (16), with Cu–O distances of 1.98, 2.02, and 2.81 Å (all $\times 2$) at room temperature. The Cu–O bond lengths are 1.972 Å in $Nd_2CuO_4$ (17), a so-called T′ phase in which the square-planar geometry of Cu is better defined.

The remaining compounds ($Sr_4CuIr_2O_9$ (B), $Ba_4CuIr_2O_9$, and $Ba_4ZnIr_2O_9$) are all incommensurate along [001] and their composite structures cannot be simply described in terms of mixed layer sequences. They can be considered to consist of two substructures, characterized by the unit cell parameters $c_1$ and $c_2$, where $c_1/c_2$ is not a rational fraction. Previous studies on related systems (18, 19) have identified $c_1$ as being characteristic of the columns of $A$ cations, Sr or Ba in the present case, which lie between the chains of transition metal polyhedra, the periodicity of the latter being characterized by $c_2$. For all the compositions described above, $c_1/c_2 \sim 1.5$ and commensurate $Sr_4CuIr_2O_9$ (A) can be considered a special case where $c = 2c_1 = 3c_2$, that is $c_1/c_2 = 3/2$. In fact, the magnitude of the ratio $c_1/c_2$ can vary widely, with certain special values corresponding to commensurate phases in the $A_{3n+3}A'_nB_{n+3}O_{6n+9}$ family of compounds. This can be understood by considering the general case in which the commensurate unit cell parameter ($c$) is related to $c_1$ and $c_2$ as follows:

$$c = pc_1 = qc_2;\ c_1/c_2 = q/p \qquad \text{where } p \text{ and } q \text{ are integers.}$$

The value of $c_1$ is largely determined by the size of the cation $A$, and it represents the mean separation of alternate $A_3O_9$ or $A_3A'O_6$ layers. There are therefore $2p$ pseudo-close-packed layers per unit cell, the factor of 2 arising, in effect, because of the *aba* nature of the hexagonal stacking. $c_2$ is the mean separation of the $A'$ and $B$ cations in the chains of polyhedra and $q$ is therefore the number of cations to be accommodated per unit cell in each chain, in either prismatic or octahedral sites. Each $A_3O_9$ layer provides one octahedral site per chain, but the insertion of an $A_3A'O_6$ layer generates a prismatic site which takes up twice the space (parallel to $z$) of an octahedral site. If we assume that all the sites in a chain are to be filled, then if $q < 2p$ we must utilize $2p - q$ prismatic sites and $2q - 2p$ octahedral sites to have a total of $q$ sites, all filled. The unit cell of the 2H perovskite ($n = 0$) has two layers and two transition metal cations per chain per unit cell, and therefore $p = 1$, $q = 2$, and $q = 2p$; no prismatic sites are formed and the structure contains only $A_3O_9$ layers. At the other extreme, the thermodynamic product in the Sr systems described in this

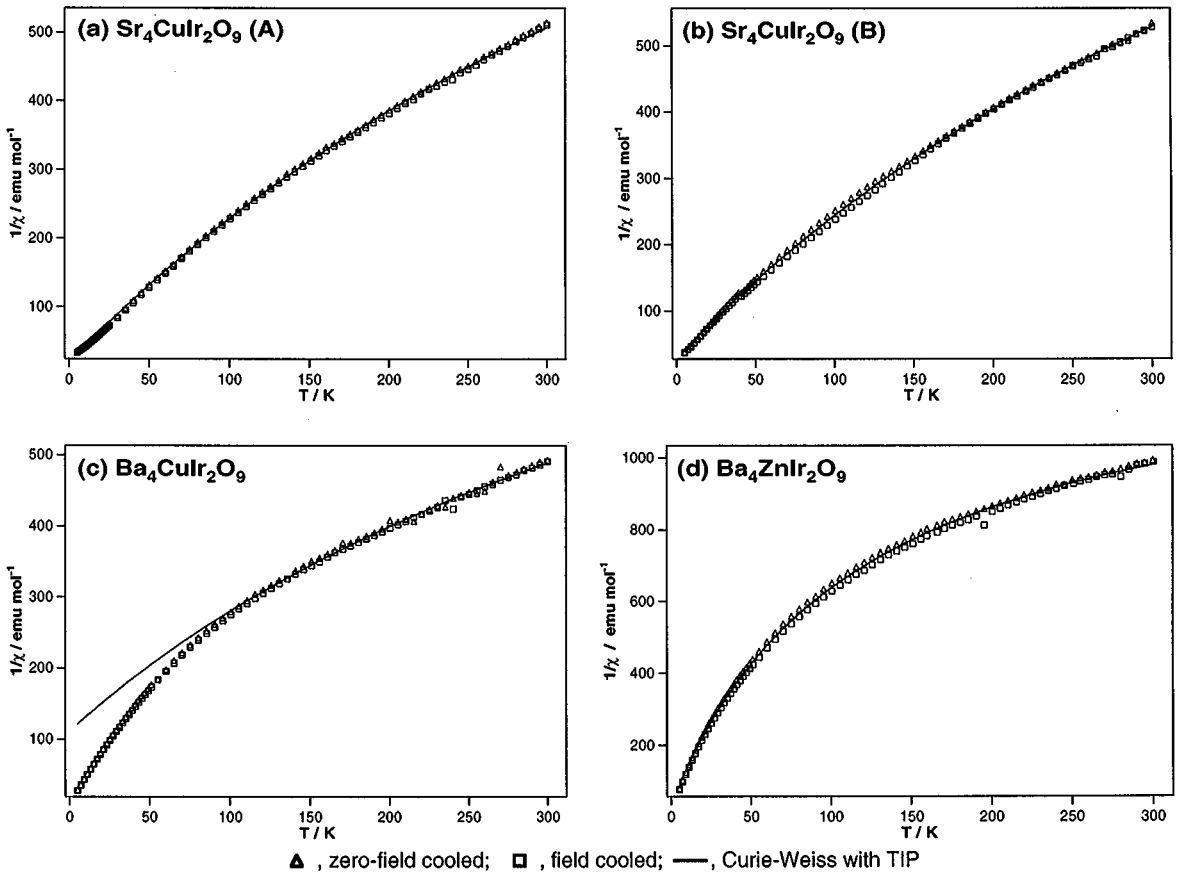


**FIG. 9.** Temperature dependence of the inverse ZFC and FC molar magnetic susceptibilities of (a) $Sr_4CuIr_2O_9$ (A), (b) $Sr_4CuIr_2O_9$ (B), (c) $Ba_4CuIr_2O_9$, and (d) $Ba_4ZnIr_2O_9$. Fits to a modified Curie–Weiss law are shown.

paper, $Sr_3A'IrO_6$ ($n = \infty$), has six layers and four cations per chain per unit cell (14); therefore $p = 3$, $q = 4$, $q = 4p/3$, and equal numbers of octahedral and prismatic sites are utilized. These two limiting cases demonstrate that $(4p/3) \leq q \leq 2p$. For the $A_4A'Ir_2O_9$ ($n = 3$) compounds, $p = 2$, $q = 3$, and we expect $c_1/c_2 = 3/2$ for a commensurate phase; deviations from this value indicate an incommensurate structure. In a similar way, the $n = 1$ structure adopted by $Ba_6CuIr_4O_{15}$ has $c_1/c_2 = 5/3$ (20), whereas the related incommensurate compound $Ba_6ZnIr_4O_{15}$ has $c_1/c_2 = 1.63$.

**TABLE 7**
**Magnetic Susceptibility Parameters for $A_4A'Ir_2O_9$**

| Compound | $C$ (emu K mol$^{-1}$) | $\Theta$ (K) | $\alpha \times 10^4$ (emu mol$^{-1}$) |
|---|---|---|---|
| $Sr_4CuIr_2O_9$ (A) | 0.396 | − 7.5 | 6.85 |
| $Sr_4CuIr_2O_9$ (B) | 0.384 | − 11.8 | 6.60 |
| $Ba_4CuIr_2O_9$ | 0.398 | − 49.4 | 9.06 |
| $Ba_4ZnIr_2O_9$ | 0.086 | − 3.45 | 7.37 |

The evolution of $c_1/c_2$ during the synthesis of $Sr_4CuIr_2O_9$ illustrates the flexibility of the system. After 1.25 h an intermediate having $c_1/c_2 = 1.504$ had formed; on heating for a further 3.75 h, it became commensurate (3/2), and then, after 4 days, incommensurate again, this time with $c_1/c_2 < 1.5$. Finally, on prolonged heating, a commensurate $n = \infty$ phase was formed, with a minimum $c_1/c_2 = 4/3$. These reactions were very fast by the standards of solid-state synthesis, at least when a 1-g sample was being prepared; it took somewhat longer to prepare a homogeneous 8-g sample for the neutron diffraction experiments. In our studies of Ba-containing compounds we did not observe $c_1/c_2$ ratios lower than $\sim 1.55$. We attribute this to the relatively large size of Ba and the large values of $c_1$ to which this gives rise. $Ba_3NaIrO_6$, in which the prismatic site is occupied by $Na^+$, has been prepared (21), but it seems unlikely that it will be possible to prepare commensurate Ba-containing $A_{3n+3}A'_nB_{n+3}O_{6n+9}$ phases with $n > 2$ ($c_1/c_2 = 14/9$) where $A'$ is a transition metal. The origin of the incommensuration

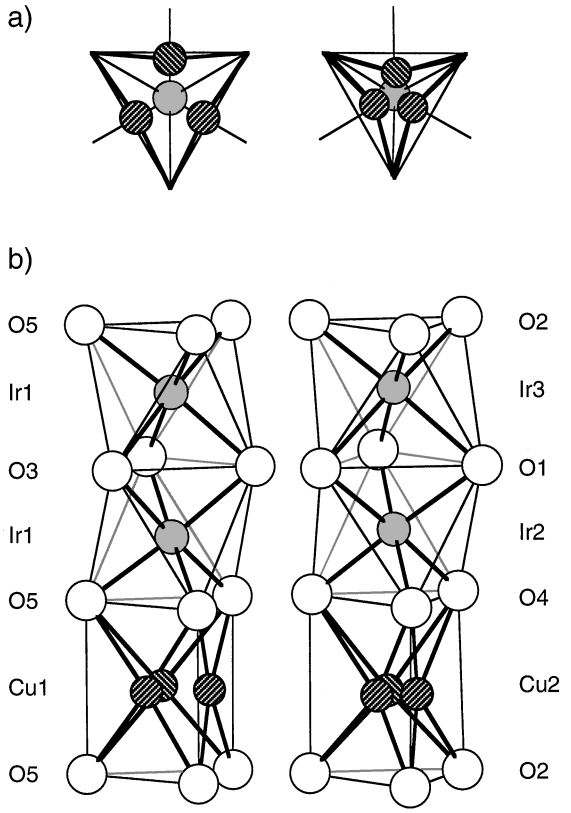


**FIG. 10.** Local coordination around Ir and Cu cations in $Sr_4CuIr_2O_9$, viewed (a) parallel and (b) perpendicular to [001].

in these structures remains an open question. Any change in composition between samples A and B of $Sr_4CuIr_2O_9$ was smaller than the uncertainties associated with our analytical methods. By analogy with $Ba_x(Cu, Pt)O_3$ (19) and $Sr_{1.145}TiS_3$ (22), there may be a pseudoperiodic rotation of the triangles of oxide ions along $c_2$, which in turn produces a modulation of Sr or Ba positions along $c_1$. However, a detailed consideration of diffraction intensities is needed before this issue can be resolved. It is interesting that the magnetic properties of the Ir oxides described above are apparently insensitive to the $c_1/c_2$ ratio. It remains to be seen whether this is the case in compounds of other 4*d* and 5*d* transition metals.

## ACKNOWLEDGMENTS

We are grateful to the EPSRC for financial support, to R. M. Ibberson for experimental assistance at Rutherford Laboratory, and to J. Darriet and F. Weill for useful discussions.

## REFERENCES

1. T. N. Nguyen, P. A. Lee, and H.-C. zur Loye, *Science* **271,** 489 (1996).
2. J. Darriet and M. A. Subramanian, *J. Mater. Chem.* **5,** 543 (1995).
3. J. J. Lander, *Acta Crystallogr.* **4,** 148 (1951).
4. C. Dussarrat, J. Fompeyrine, and J. Darriet, *Eur. J. Solid State Chem.* **32,** 3 (1995).
5. J. A. Campa, E. Gutiérrez-Puebla, M. A. Monge, I. Rasines, and C. Ruíz-Valero, *J. Solid State Chem.* **108,** 230 (1994).
6. W. T. A. Harrison, S. L. Hegwood, and A. J. Jacobson, *J. Chem. Soc., Chem. Commun.* 1953 (1995).
7. J. Campá, E. Gutiérrez-Puebla, A. Monge, I. Rasines, and C. Ruíz-Valero, *J. Solid State Chem.* **126,** 27 (1996).
8. M. Strunk and H. Müller-Buschbaum, *J. Alloys Compd.* **209,** 189 (1994).
9. F. Abraham, S. Minaud, and C. Renard, *J. Mater. Chem.* **4,** 1763 (1994).
10. P. A. Stadelman, *Ultramicroscopy* **21,** 131 (1987).
11. H. M. Rietveld, *J. Appl. Crystallogr.* **2,** 65 (1969).
12. A. C. Larson and R. B. von Dreele, "General Structure Analysis System (GSAS)," Report LAUR 86-748, Los Alamos National Laboratories, 1990.
13. P. D. Battle and J. G. Gore, *J. Mater. Chem.* **6,** 1375 (1996).
14. A. V. Powell, P. D. Battle, and J. G. Gore, *Acta Crystallogr.* **C49,** 189 (1993).
15. J. Darriet, J. L. Soubeyroux, and A. P. Murani, *J. Phys. Chem. Solids* **44,** 269 (1983).
16. M. Neubacher and H. Müller-Buschbaum, *Z. Anorg. Allg. Chem.* **607,** 124 (1992).
17. H. Müller-Buschbaum and W. Wollschläger, *Z. Anorg. Allg. Chem.* **414,** 76 (1975).
18. T. Shishido, K. Ukei, and T. Fukuda, *J. Alloys Compd.* **237,** 89 (1996).
19. K. Ukei, A. Yamamoto, Y. Watanabe, T. Shishido, and T. Fukuda, *Acta Crystallogr. B* **49,** 67 (1993).
20. P. D. Battle, G. R. Blake, J. Darriet, J. G. Gore, and F. Weill, *J. Mater. Chem.* **7,** 1559 (1997).
21. S. Frenzen and H. Müller-Buschbaum, *Z. Naturforsch.* **51b,** 1204 (1996).
22. M. Onoda, M. Saeki, A. Yamamoto, and K. Kato, *Acta Crystallogr. B* **49,** 929 (1993).